3D analysis of enamel demineralisation in human dental caries using high-resolution, large field of view synchrotron X-ray micro-computed tomography

Cyril Besnard [a],*, Robert A. Harper [b], Thomas E.J. Moxham [a,c], Jonathan D. James [b], Malte Storm [c,1], Enrico Salvati [a,2], Gabriel Landini [b], Richard M. Shelton [b], Alexander M. Korsunsky [a]

[a] MBLEM, Department of Engineering Science, University of Oxford, Parks Road, Oxford, Oxfordshire, OX1 3PJ, UK
[b] School of Dentistry, University of Birmingham, 5 Mill Pool Way, Edgbaston, Birmingham, West Midlands, B5 7EG, UK
[c] Diamond Light Source Ltd., Didcot, Oxfordshire, OX11 0DE, UK

ARTICLE INFO

ABSTRACT

We report major advances in the analysis of synchrotron 3D datasets acquired from human healthy and carious dental enamel. Synchrotron tomographic data for three human carious samples and a non-carious reference tooth sample were collected with the voxel size of 325 nm for a total volume of $815.4 \times 815.4 \times 685.4$ μm^3. The results were compared with conventional X-ray tomography, optical microscopy, and focused ion beam-scanning electron microscopy. Clear contrast was seen within demineralised enamel due to reduced mineral content using synchrotron tomography in comparison with conventional tomography. The features were found to correspond with the rod and inter-rod structures within prismatic enamel. 2D and 3D image segmentation allowed statistical quantification of important structural characteristics (such as the aspect ratio and the cross-sectional area of voids, as well as the demineralised volume fraction as a function of lesion depth). Whilst overall carious enamel predominantly displayed a Type 1 etching pattern (preferential demineralisation of enamel rods), a transition between Type 2 (preferential inter-rod demineralisation) and Type 1 was identified within the same lesion for the first time. This study does not provide extensive results on the different lesions studied, but illustrate a new method and its potential application.

1. Introduction

Caries is a major worldwide disease [1] that affects the well-being of millions of individuals due to damaging dental hard tissues. In 2017 it was reported that the prevalence caries in permanent teeth without the world population reached around 2.3 billion [2]. In addition to discomfort, pain and loss of productivity due to caries, the significant economic burden amounting to billions of US dollars worldwide arises through the necessity to provide treatment [3]. The evolution of enamel demineralisation in a carious lesion is intricately linked to the interaction between acid diffusion and hydroxyapatite (HAp) dissolution

processes. The acid is generated due to the presence and activity of bacterial species *e.g. Streptococcus mutans* within biofilms known as dental plaque [4–8]. At present, no effective methods are available to fully regenerate tissues to reverse the damage caused by caries. To a significant part, this is due to the lack of sufficiently detailed understanding of the process of demineralisation (and remineralisation) of the fine structure of dental tissues. For the tissue that is most important in this context, enamel, there is a lack of detailed observation and ability to predict the course of these processes through numerical simulation. Although some encouraging progress has been reported recently [9,10], there remains an overriding need for nano- to micro-scale visualisation

of caries progression. Synchrotron X-ray micro-computed tomography offers an uniquely useful tool for tackling this task. This study contributes to the clarification of these aspects by means of synchrotron X-ray micro-computed tomography and detailed three-dimensional (3D) image segmentation and analysis revealing sub-micron resolution over a millimetre size field of view. Imaging, resolving and analysing the rod and inter-rod phases of the carious enamel in three-dimensions (3D) using X-ray tomography has not previously been reported to our knowledge, and this paper attempts to illustrate this with unique visualisation techniques that enable further studies of the demineralisation and remineralisation of enamel. This study aims to provide a new method to analyse enamel or mineral tissue in high-resolution using correlative analysis.

Teeth are developmentally complex organs composed of distinct parts: a soft tissue (dental pulp) [11], surrounded by a cell-maintained moderately mineralised tissue, dentine, which in turn is surrounded by cementum (with similar characteristics to bone [12]) in the dental root(s), and highly mineralised enamel (mineral 85 % by volume, and a low percentage of protein, lipid and water [13,14]) forming the outer shell of the tooth crown [15]. Recently, using mice incisors, Bai et al. described the role of the protein nanoribbons in the formation of the crystals in the enamel [16]. Enamel is composed of plate-like HAp nanocrystallites, which can be ~30 nm in width and ~70 nm in thickness on average, and more than 100 μm in length [9,17], with the major axis along the c-axis. HAp crystallites are arranged into larger elongated 'prisms' (also referred to as *rods*) around 5−6 μm in diameter [18–22]. The prisms are joined together by an organic region called the prism *sheath* [23–26]. The interprismatic regions (*inter-rod*) that lie between enamel prisms are around 1−3 μm in thickness [17,27–29], and Kelly et al. study of 28 individuals, found inter-rod thickness was between 1 and 5.7 μm (average of 2.9 μm) [30]. At the free surface of enamel, a prism-less region can sometimes be present, also referred to as 'aprismatic' enamel [31–33]. In this study, we followed the nomenclature of Ten Cate [34] with regards to the term *prism* not being used due to the irregular shape of the rods. Important features of hierarchical enamel organisation are striae of Retzius (SR) and Hunter-Schreger bands (HSBs). SR result from temporal variations in the secretory activity of ameloblasts during enamel formation [35–37] with an arrangement described as a 'staircase' structure with a spacing that increases from the tooth surface [31,38] from ~15−20 μm in the cervical enamel to ~25−35 μm in the mid-enamel location [39] and spacing ranging from 25 to over 150 μm [40]. Using synchrotron tomography, Dowker et al., analysed the 3D structure of the SR in samples with lesion [41].

HSBs are observed in enamel due to the change in the enamel rod direction that produces a 'weave' effect. This change in direction is thought to improve enamel resistance to cracking [42,43]. HSBs can be visualised using several techniques such as optical microscopy [44], and synchrotron X-ray high-resolution holotomography using phase contrast [45] (from the enamel of a rhinoceros).

The aspects of the hierarchical structure of human teeth from submicron to the millimetre scale is described, Supplementary Information 1 (SI-1) Fig. S1 and determines its outstanding properties, namely, the resistance to fracture, wear, chemical attack and thermal shock under the extreme conditions arising in the oral cavity. The principal aspect of vulnerability of dental enamel lies in it being prone to demineralisation by acids that may lead to reduction in mechanical strength, structure modification and potential caries formation [29,37, 46–53]. The interest for the present investigation is *enamel caries*.

Demineralisation of enamel, either artificially or due to caries, leads to different features that can be classified according to their progression. Five types of etching pattern have been reported, *e.g.* type 1 demineralisation (where rod centres are preferentially demineralised) or type 2 (with demineralisation of the inter-rod substance) [54,55]. Atomic force microscopy and scanning electron microscopy (SEM) are used to distinguish the location of the demineralisation due to their high-resolution [18,54–56]. The demineralisation process is not

identical across different individuals, genetic variation could modulate the risk of caries *via* developmental and structural modifications of the enamel [30]. Mortimer and Tranter [57] suggested that enamel demineralisation in caries occurred along the enamel rods in early stages and then propagated to the core and sheath. Simmelink and Nygaard observed using transmission electron microscopy (TEM) cross-striations in a carious sample [58]. Using TEM, the periphery of the rods was found preferentially more dissolved than the core of the rod at early stages [59, 60]. Demineralisation, formation and restoration of enamel crystals were observed using high-resolution TEM analysis on carious lesions [61].

To analyse enamel caries and artificial demineralisation, research has been done using synchrotron-based methods (X-ray fluorescence, wide- and small-angle X-ray scattering, X-ray diffraction and micro-computed tomography [10,62–69]). That has provided detailed information about X-ray absorption, structure, crystal size and preferred orientation, as well as composition *via* elemental, chemical, structural, and physical analyses. The ability of tomography to demonstrate large volumes of tissue compares favourably with *e.g.*, confocal laser scanning microscopy which can identify proteins and bacteria, but has limited penetration depth in mineralised tissues [70,71]. Focused ion beam - SEM has been used extensively due to its high-resolution and possibility of the combination with energy-dispersive X-ray spectroscopy for 3D elemental mapping. However, the addressable 3D field of view is constrained by the large milling time to reach tens of microns [72–74]. Recently using atom probe tomography (APT) analysis in combination with TEM and fast Fourier transformation on carious and sound enamel, locations where the lesions preferentially occurred was studied [75]. Three distinct locations were found: along a central dark line (Reyes-Gasga et al. [76]), in organic-rich precipitate and at grain boundaries of HAp with high angles (90° and 113.5°). These studies were the first to characterise impurities in enamel caries at the nano-scale. In another study, using APT for the distribution of elements in enamel, density functional theory and X-ray diffraction for the lattice parameters and then finite element modelling, preferential dissolution in the core region was suggested to arise from residual stress caused by chemical gradients [9]. The formation of the gradient was suggested to originate from amelogenesis and enamel maturation stages. Carious lesions were also characterised using high-energy X-ray diffraction computed tomography and diffraction patterns, where amorphization in the lesion was identified [69].

Investigation of enamel caries lesions using conventional X-ray micro-computed tomography has provided data at the micron-scale restricted by a compromise between the field of view and resolution (see this study). A summary of a review of the 3D analyses carried out on human teeth (principally) is given in Supplementary Information 2 (SI-2) with details on resolution, date and dimension and an overview of applications (SI-2 Table S1 and Figs. S1,2). We exploit the potential of high-resolution synchrotron X-ray micro-tomography to analyse carious enamel with the help of several supplementary techniques, including conventional micro-computed tomography, optical microscopy and scanning electron microscopy with focused ion beam, to achieve a multi-modal, multi-scale characterisation going beyond radiography. To the best of our knowledge, this is the first report of enamel carious lesions at high-resolution ($0.3 \times 0.3 \times 0.3$ μm^3) performed with isotropic voxels and a large field of view (0.83×0.7 mm) to allow detailed segmentation and statistical analysis of volumetric data. This provides innovative methods to analyse enamel, however, more samples are required for systematic comparison of the results illustrated in this manuscript.

2. Materials and methods

2.1. Sample preparation for tomography

The study used intact and anonymised actual human third molars extracted for non-caries related therapeutic reasons at the School of

Dentistry, University of Birmingham (ethical approval obtained from the National Research Ethics Committee; NHS-REC reference 14/EM/1128/ Consortium Reference BCHCDent332.1531.TB). Teeth were cut into blocks of roughly rectangular shape using a 4-inch diameter low speed diamond saw (Buehler IsoMet®, U.K.). For the samples prepared, enamel thickness in the z direction (perpendicular to the occlusal surface) was around 0.5 mm, whilst the perpendicular dimensions were ~1.5 mm in the x direction and greater than ~0.8 mm in the y direction. Five human teeth were studied in total: one advanced enamel caries with two samples (AEC1 and AEC2), one sample from a less advanced early enamel caries, *i.e.* early smooth surface caries of enamel now on referred to as 'enamel caries' (EC1), a third tooth with two samples of enamel each containing an artificially demineralised region using lactic acid at a different pH (NC1 and NC2), with NC1, which was used for reference and control with intact health enamel region, a fourth tooth with three samples of enamel also demineralised at different pH (NC3, NC4, and NC5), and a fifth tooth with one sample treated with lactic acid (NC6). These additional demineralised samples were used to confirm the details seen with SR X-ray μCT. To induce local demineralisation, commercially available nail varnish was applied on NC1-6 to protect the block surface, with a small area left exposed to acid attack. The acid treatment was done by exposing the varnished teeth to lactic acid (0.5 % v/v, 0.5 mL) at 37 °C for a duration of three weeks, different pH conditions were used, pH 4, 4.4, 4.8 and 5.2. Every two days the solution was changed to keep a similar environment. Since the samples were anonymised, no information about age, sex ethnicity or dietary habits of the individuals was available. Caries assessment was carried out by visual inspection by a dentist.

2.2. Sample preparation for structure comparison between rod and inter-rod phases

Sections of human dental enamel were prepared with 150 μm thickness slices were taken with the tooth clamped in its 'native' orientation *i.e.*, as it would be present in the mouth. The first slice of surface enamel was discarded (as potentially aprismatic) and the next slice was processed using the cutting equipment mentioned earlier and polished (with a wet stone). One of these samples was etched by submersion in 2 % lactic acid for 2 h then rinsed with water and stored in phosphate-buffered saline (PBS) solution before analysis, and another sample was kept as a reference without etching. The two slices were coated with gold (Au) and palladium (Pd) with a thickness of ~5 nm using SC7620 sputter coater (Quorum Technologies, U.K.), and conductivity ensured with silver paint to the stub. The etched sample was analysed using SEM Tescan Lyra 3 (Tescan, Czech Republic) with secondary electron acquisition and backscatter detector inserted, using a 5 keV electron beam. Additional details of the human enamel sections were also reported in [117].

2.3. Optical microscopy

The AEC2 sample was placed on a glass slide and analysed using a polarising light microscope (Primotech, Zeiss, Germany) in transmission illumination mode. Images were captured using a digital camera with an Epiplan 5X objective that provided a field of view of ~2300 × 1725 μm (2048 × 1536 pixels). AEC2 was also analysed with Alicona Infinite focus optical profilometer (Alicona Imaging GmbH, Austria) using imaging mode with and without polarizer. The objectives used were from 5 to 20X with a field of view of 1624 × 1232 pixels (~2847 × 2159 μm to ~711 × 539 μm respectively). The sample was analysed with and without deionised water cleaning following PBS storage. The sample was fixed on a SEM aluminium stub before the focused ion beam (FIB)-SEM preparation, and then was observed on carbon tape after FIB-SEM. In addition, X-ray micro-computed tomography data was collected (Fig. 1a and SI-1 Fig. S7).

2.4. FIB-SEM – SEM AEC2 and reference sample

AEC2 was initially imaged without deionised water cleaning, stored in PBS and then cleaned with deionised water for FIB-SEM analysis. AEC2 was characterised using FIB-SEM at five locations on one side of the carious enamel. FIB-SEM analysis was done using SEM Tescan Lyra 3 (Tescan, Czech Republic) and FIB with a gallium source, the stage was tilted at 55° for the FIB process. A beam voltage of 30 keV and an emission current of 2 μA were used. For cross-section analysis, large trenches were made using the integrated 3D acquisition wizard from the Lyra software, followed by a thinning process (probe current ~195-235 pA). The thinning was done using the 3D acquisition wizard and thinning with several slices of ~29 nm and with additional thinning (rectangular shape) if required. Normal enamel was also characterised using milling and thinning with a slice thickness of ~29 nm to compare the cross-sections. In both samples, an initial platinum (Pt) deposition and marker for drift correction were set. These cross-sections were then imaged using SEi and BSi with 5 keV, similar to other locations of AEC2. The BSi of one location of the carious sample was filtered, segmented and analysed in two-dimensions (2D) to quantify the porosity using Avizo software. Images from microscopy were analysed using Avizo, colour maps were adjusted as necessary to maximise clarity.

EAC2 was also coated with 10 nm Au/Pd after that a few cross-sections were made (Locations 1-5 from SI-1 Fig. S12), and the SEi and BSi were taken with 10 keV. The Euclidian distance between voids was computed from the BSi after applying a median filter, and then performing the segmentation of the region between voids using 'interactive thresholding' (Avizo software v2020-1) for each location analysed. Additional details on the computation are mentioned in the micro-computed tomography analysis

From the FIB process of the cross-sections of AEC2, a comparison was made with the probe current used during the thinning process using three settings. The sample was coated with an additional 10 nm Au/Pd, and silver paint was spread on the edge of the sample and the carbon tape and SEM stub. Then the FIB process was carried out and compared with a location in the reference section enamel.

2.5. X-ray micro-computed tomography (X-ray μCT)

Two types of X-ray micro-computed tomography were used to generate a multi-resolution description of the enamel caries lesions, namely, conventional (using laboratory X-ray sources) and synchrotron-based versions. Synchrotron X-ray micro-computed tomography (SR X-ray μCT) was used to study fine sub-micron details of enamel structure and its modification due to demineralisation in comparison with lower resolution of the conventional micro X-ray micro-computed tomography (Conv X-ray μCT).

The Conv X-ray μCT data collection of AEC2 was done through white beam absorption contrast projections using a Skyscan 1172 instrument (Bruker, Belgium) over 360° angular range with rotation steps of 0.2° and averaging over six frames (at room temperature). An excitation voltage of 60 kV and current of 167 μA were used. A 0.5 mm-thick aluminium filter was used to 'harden' the beam, and the detector pixel size of 1.51 μm and a field of view of 6.04 × 4.022 mm (4000 × 2664 pixels) for the projections. Similarly, NC3 was analysed with reconstructed dataset of 3198 × 778 pixels.

Synchrotron tomography analysis of NC1-6, AEC2, AEC1 and EC1 was carried out at Beamline I13-2, the Diamond Manchester Imaging Branchline [77–79] (Diamond Light Source, Oxford Harwell Campus, Didcot, U.K.). Projections were collected in parallel beam geometry in the range between 0° and 180° with an exposure time of 0.3 s and angular step of 0.05° at room temperature. A pink beam was used with an average energy of 21.8 keV. The scintillator screen was positioned at a distance of approximatively 45 mm from the sample. The detector used was a pco.edge 5.5 (PCO AG, Germany) CMOS sensor with a 10X objective lens and a total magnification of M = 20X that provided the
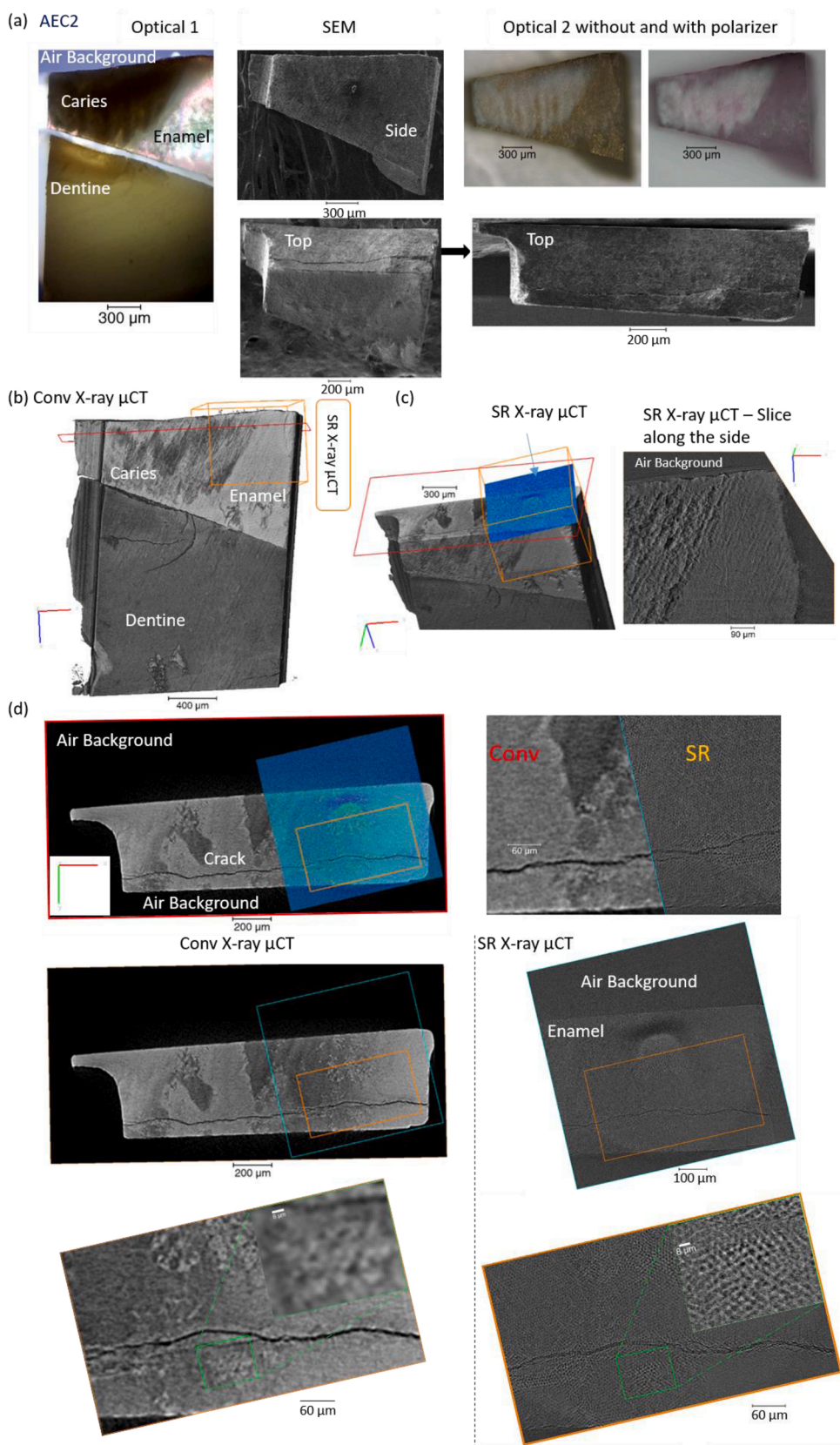
Fig. 1. Comparison of different techniques in the analysis of AEC2 for one side using microscopy and volume using tomography. (a) Optical polarised light image (referred to as Optical 1), SEM images of the top and side of the sample, and optical image with and without polarizer using profilometer equipment (referred to as Optical 2). (b-d) correlation of the two tomography dataset, (b) 3D rendering of the Conv X-ray μCT analysis with an overlap of the dimension of the SR X-ray CT data, (c) overlap of an extracted slice of SR data with the volume of the Conv X-ray μCT (in red slice which will be used for comparison) and additional slice from the synchrotron data (showing the side of the sample), and (d) comparison of two extracted slices displayed in (c), with red for the Conv X-ray μCT. A juxtaposition of the two slices is displayed and then for each case shown, xy plane section view is extracted from the 3D dataset, and magnified views are shown. For the last subregions, scale bar 8 μm. In SI-1 Fig. S3b, the other side of the sample is compared. The crack observed was used to correlate the locations in the two tomograms. The colour map for the SR X-ray μCT data was used to display the slice and its location. (For interpretation of the references to colour in the Figure, the reader is referred to the web version of this article).

pixel size of 0.325 μm and a field of view of 0.83 × 0.70 mm. Lens distortions were corrected using correction coefficients acquired from a dot field array [80].

Apart from resolution, the acquisition time varied significantly between laboratory and synchrotron scans: data collection took 7 h for Conv X-ray μCT, while for SR X-ray μCT took less than 30 min per sample.

The images acquired are based on the X-ray absorption by the tissue and contrast can be observed on the detector according to the variation of composition in the volume acquired, which is based on Lambert-Beer's Law [81]. This difference in contrast can therefore be used to identify the demineralised zone in the tissues analysed.

2.6. 3D reconstruction of X-ray μCTs

Laboratory X-ray μCT reconstruction was performed using NRecon software (Bruker) in a similar way as previously study [44]. From the reconstruction, 1556 slices perpendicular to the rotation axis were obtained, a dimension of 1376 × 472 pixels for each. The resulting 3D dataset was characterised by isotropic voxels of 1.51 μm in size and for a volume of 1376 × 472 × 1556 pixels (2076 × 711 × 2348 μm^3).

3D reconstruction of the SR X-ray μCT data was carried out using Savu software (Diamond Light Source, U.K.) with the help of bespoke plugins [82,83]. Dark images (to remove the effect of the detector readout noise) and flat-field images (to remove the effect of the scintillator and beam profile) were captured prior to acquisition for each sample and used for projection normalization. The centre of rotation was manually optimised based on the minimization of artefacts. Distortion correction and ring removals were applied before reconstructing the data using the Tomopy implementation in Savu [84].

The reconstruction produced 2110 slices perpendicular to the rotation axis with the dimension of 2510 × 2510 pixels each. The resulting 3D data set was characterised by isotropic voxels of 0.325 μm in size. Overall, four enamel samples were analysed.

The interpretation of SR X-ray μCT projections images with line analysis and 3D volumetric image data segmentation was carried out using Avizo v2019 and v2020-1 software (Thermo Fisher Scientific, USA) [85]. Image analysis and observation of reconstructed dataset, extraction and cropping of regions were performed with ImageJ-Fiji image analysis software (ImageJ, NIH, Bethesda, MA, USA) [86–88] and Avizo. The flow diagram from projection to reconstruction and segmentation of the synchrotron data is shown in SI-1 Fig. S2. Complete synchrotron datasets corresponded with the volume of 815.4 × 815.4 × 685.4 μm^3. A detailed interpretation was carried out for sub-regions (due the computational limitations) for instance of 500 × 500 × 1054 voxels, corresponding with a ~162 × 162 × 342 μm^3. One of the regions of interest (ROI) location from the full dataset of AEC1 is indicated in Fig. 3. For each 3D rendering, the scale bars were from a two-dimensional (2D) view perpendicular to the viewing direction, and in many figures, the volume of the analysis was mentioned, with the axis.

3D image segmentation and interpretation were proceeded with several steps described in SI-1 Note 1 and SI-1 Fig. S2b. In the study of the lesion segmented, sub-regions were defined using labels that corresponded to low density (voids within the lesion) within the remaining enamel tissue. This allowed structural statistical analysis to be performed. For 2D image analysis (slice per slice analysis), statistical data was extracted for several parameters including area (the interpixel distance was 0.325 μm, and the area was measured in pixel squared units), maximum Feret's diameter [89] (referred to as 'length') and density profile within the lesion (*Density*), defined as the ratio of void area (lesion segmented $A_{segmented}$) to the overall enamel section area A_{enamel}, which for one slice was computed as (Eq (1)):

$$\begin{cases} Density\ \% = \dfrac{A_{segmented}}{A_{enamel}} \\[2mm] A_{segmented} = \sum_{k=1}^{n} A_{individual} \end{cases} \tag{1}$$

Where n is the maximum number of individual connected pixels segmented, k is the index, and $A_{individual}$ is the respective area.

For 3D characterisation, 3D rendering data was analysed to extract further statistical parameters, including void volume, the maximum and minimum Feret's diameters (corresponding with the length 3D and width 3D, respectively) and the 3D Feret aspect ratio (defined by the ratio of these two parameters and noted 'Feret shape'). Additionally, the spacing between voids and the maximum diameter of a sphere within individual voids were calculated using the thickness map module from Avizo (referred to as 'thickness' in μm). This implements an approach according to which the maximum diameter of a sphere is found that fits in a void, following the work of Hildebrand and Rüegsegger [90]. The spacing between demineralised regions (referred to as 'non-demineralised') was analysed using the Euclidean distance metric (this will be referred to as 'distance' in μm, and was calculated using the distance map module from Avizo). Colour maps were used to visualise the 2D and 3D dataset. Some 3D datasets were reduced using the 'filter by measure range' module from Avizo which extracted the data from a range of values, this was done for the volume, and for the Feret shape. In many figures, the number were rounded. Line profile analysis of the grey values of the projections of AEC1, AEC2 and NC1, and of the 3D reconstruction of the three carious samples was done using line probe module implemented in Avizo with a step of 0.325 μm and with interpolation.

The graphs presented were generated using Matlab (The MathWorks, Inc., USA) and OriginPro (OriginLab Corporation, USA).

3. Results – discussion

3.1. SR X-ray μCT data and conventional analysis using optical microscopy and X-ray μCT

In Fig. 1a, the optical polarised light analysis is shown and the carious region is visible as a dark area within the enamel (sample AEC2). The same side was observed using SEM with additionally the top of the sample used to correlate with the tomography data. Optical images were also taken with the second equipment and highlighted the carious region with different colour. Fig. 1b-d shows the Conv X-ray μCT tomographic image within AEC2 tooth slice and this was compared with the volume of the synchrotron analysis Fig. 1c and slices Fig. 1c-d (additional comparison of the projections, of another slice, and another view of AEC2 is illustrated in SI-1 Fig. S3a,b). Micron-scale resolution was only observed for the synchrotron data and the contrast was enhanced between the lesion and less demineralised area, with clear identification of rod demineralisation, corresponding with the type 1 etching pattern. This level of detail was used to analyse further the synchrotron data with the possibility to identify individual void (additional details on the resolution of synchrotron in comparison with conventional techniques, see SI-1 Note 2). The comparison of the two techniques was also done on an etched sample NC3 with similar conclusions on the resolution obtained see SI-1 Note 2, SI-1 Fig. S3c.

3.2. Analysis of reconstructed slices from the xy, xz and yz orientation which are from the sample position

3D rendering of the scans of samples AEC1, AEC2, and NC1 with additional subset slices along the xz and xy planes showed the difference in the contrast of the enamel between advanced carious lesions and NC1 (see SI-1 Fig. S5). The difference could also be seen only by looking at the raw projections (details in SI-1 Note 3 SI-1 Figs. S6,7), where the

demineralisation region was observed in contrast to the sound enamel structure where mineralised density difference in the structure was not enough to determine rods, and this was also illustrated on the side of the carious samples AEC2 (SI-1 Fig. S6d).

3D rendering of the scans of samples AEC1, AEC2, and NC1 with additional subset slices along the xz and xy planes confirmed the difference seen in the projection between the advanced carious lesion and NC1 (see SI-1 Fig. S5). There were no noticeable features in the xy plane of the reference sample except the features mentioned so far (SI-1 Fig. S5c). In the two carious samples shown in SI-1 Fig. S5, similar results were observed and it revealed demineralisation which could be observed in rods and depending of the orientation of the cross-section being seen as 'holes' in the xy planes and as 'channels' in the xz plane slices. In relation to the direction of the rods, the xy plane is considered close to the perpendicular of direction of many rods. The features seen as channels were in agreement with previously reported features in back-scattered electron images [91–93].

Although direct comparisons between samples from different individuals and different environmental conditions are difficult to generalise, interestingly, in the xz plane of both samples, less demineralisation was observed near the tooth surface compared with depths of 150 µm or more, where features with voids of around 5 µm in diameter were found. This less demineralised area at the surface of the carious lesion (the so called 'surface zone') has previously been described [61,64,92,94–96] and it was confirmed here. Interestingly a similar observation has also been reported at the surface of artificially demineralised pellets of hydroxyapatite, where there is no hierarchical structure as in natural enamel, which suggests that this zone might not be a characteristic of caries only [94]. Using human saliva for the remineralisation of teeth and TEM for the analysis, Arsecularatne and Hoffman noticed subsurface remineralisation of the enamel [97]. Deposition of material at the surface of enamel has also been identified using SEM after treatment using artificial saliva on artificially demineralised region [98]. The presence of a less demineralised surface zone was also noticed using Raman analysis of artificially demineralised surface using lactic acid by studying the depth profile of phosphate peaks [99]. From the demineralisation using an oral biofilm reactor with *Streptococcus mutans* and transverse microradiography, a higher mineral density was found at the surface in comparison with subsurface of the enamel [100].

A wider area was analysed on AEC1 and from the difference in the features observed in the demineralisation region, caries advancing through the HSB was suggested. Elongated voids adjacent to less elongated from the same virtual cross-section were seen (SI-1 Fig. S10). Additionally, the curvature of the enamel rods could be visualised along the sample, and this is detailed in xz view (SI-1 Fig. S11).

In addition to the 3D reconstruction of the SR X-ray µCT data of AEC2, FIB-SEM analysis was carried out in five locations of this sample, referred to as Locations 1-5. One location was chosen outside of the lesion and this was confirmed using optical imaging and termed Location 1. Correlation was made between the cross-sections seen with FIB-SEM and slices extracted from the SR X-ray µCT dataset. It was found that there was no significant demineralisation outside the lesion compared with inside the lesion using both of the techniques. From FIB-SEM, the porosity was quantified at Location 3. The dimensions of the enamel structure observed using FIB-SEM was comparable with what was observed using the SR X-ray µCT. This correlation was shown in SI-1 Note 4 and Figs. S12-15.

3.3. Quantitative assessment of morphological features from 2D label analysis and 3D rendering

The purpose of this section was to get some statistics data about the lesion once this was isolated from the rest of the dataset and from the dimension of the non-demineralised region. The area of the carious lesion was quantified along the thickness of the sample to obtain a density profile, Eq (1), using the demineralised phase and total area of

the tooth per slice. The 3D rendering of the volume of the lesion was observed from top to bottom of the region acquired.

Three dimensional volume rendering and 2D label analysis of the mineral loss of the subregion in the AEC1 sample shown in Fig. 2 was based on a combination of segmentation by thresholding after filtering with non-local means. The labelling of the demineralised region in 2D was computed for each slice along the z-axis (full details can be found in SI-1 Note 5). Fig. 2a,b shows an example of the analysis of one slice before and after labelling. Different colours (labels) were assigned to each segmented region. The number of individual regions is displayed Fig. 2c.

Fig. 2d showed the density profile of the lesion as the percentage of many individual demineralised areas within the entire lesions at various segmentation depths divided by the total area of the enamel along the depth of the sample. From the density profile of the lesion, we were able to map the demineralisation along the depth and four distinct zones were observed and defined based on the density profile. The first zone extended from ~0−52 µm in depth with little mineral loss. The second zone, extending from ~52−131 µm in depth, presented a progressively increased in mineral loss, a third zone with a gradually decreasing mineral loss with depth while the fourth zone, deeper than 260 µm, exhibited low mineral loss. The volumes of each region are shown in Fig. 2e. This analysis illustrated the resolution of the SR X-ray µCT, and that individual regions could be analysed, however, more studies are required to analyse the 2D dimension following the orientation of the rods.

To examine the lesions in detail in 2D, an overlap was made on a SEM image taken from a region of an etched slice, and the length of one region was measured ~4 µm, in the range of the dimensions of the enamel rod which was around 5 µm considering that the value was relative to the grey value taken and the degree of demineralisation. The dimension was also consistent with the previous data found in SI-1 Fig. S5 (around 5 µm in diameter). For additional details on the comparison of SEM and SR X-ray µCT data from AEC2, see SI-1 Note 4 Fig. S15.

Furthermore, a 3D reconstruction of the mineral loss was computed in the additional slices located below the previous ROI ($162 \times 162 \times 342$ µm^3 for the first volume and $162 \times 162 \times 165$ µm^3 for the additional volume). The first volume analysed had 1054 slices, however this did not go to the last slice of the reconstructed dataset. Thus, the remaining slices to obtain the total volume, from the first slice of the tooth to the last one, were analysed. From the additionally reconstructed volume of the demineralised regions, it was found that low mineral loss was detected in the additional volume as shown in SI-1 Fig. S122.

Overall, demineralisation spanned the thickness of the enamel with more loss in certain regions, and the rods of the enamel structure were preferentially demineralised in comparison with inter-rods. A larger field was analysed as shown in Fig. 3. The analysis provided a detailed distribution of the mineral loss. (SI-1 Fig. S23 and Movie 1).

3.4. Interpretation of the three dimensional analysis of the segmented dataset of the demineralisation for the advanced caries samples

In this section, the segmented dataset for the demineralisation lesion was interpreted in 3D where each individual segmented objects of connected voxels was analysed. The spacing between the demineralisation segmented dataset was also quantified.

To examine the volume of the mineral loss and how the enamel was altered by demineralisation, the analysis in 3D of each segmented objects was computed on AEC1, with the first 3D rendering using different colours for dissimilar individual objects (Fig. 4a) and then colours assigned to the volume in Fig. 4b with a maximum value of 6726.1 µm^3. Demineralisation was observed in many locations, particularly in enamel rod with additional connections between segmented voids. The curvature of the demineralised rods in some locations and the connections between different regions along the depth were observed in 3D (SI-1 Figs. S24,25 and SI-1 Movies 2–4). The thickness of the
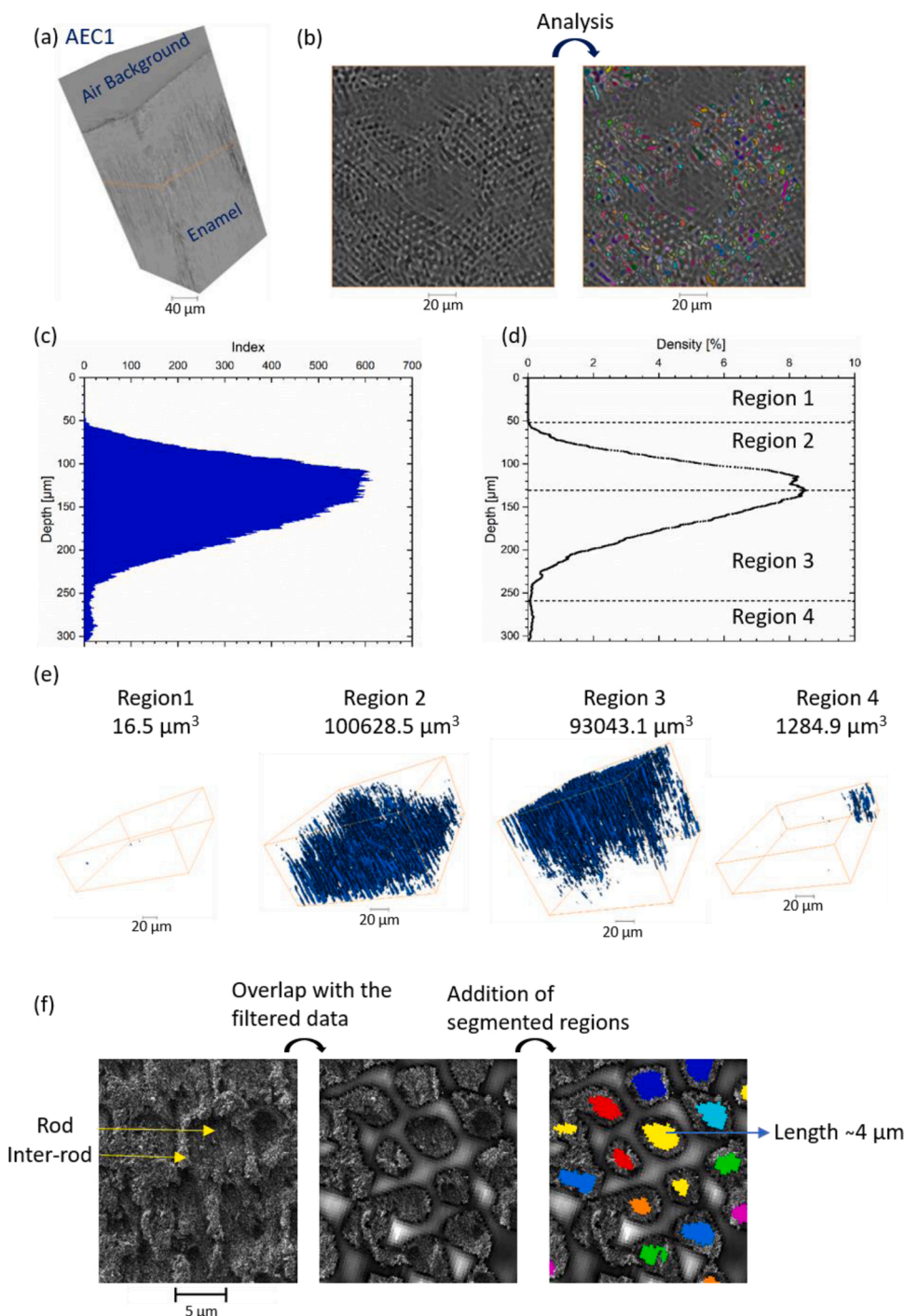
Fig. 2. 3D volume rendering (500 × 500 × 1054 pixels – 162.175 × 162.175 × 342.225 μm³) and 2D label analysis of the AEC1 sample. (a) Volume rendering of AEC1 with an extracted slice in the xy plane highlighted with an orange line, (b) extracted slice with and without analysis in 2D of the segmented dataset. (c) Quantification of the number of labels (referred as their index, each label can be computed) from the 2D analysis along the depth of the enamel, and (d) of the density of the lesion with four regions displayed. (e) Volume rendering of the four regions with the value of the volume. (f) Comparison of the region from a SEM image of an etched slice, with the filtered dataset of the enamel and the addition of the segmented region seen in (b).

demineralisation lesion is presented in Fig. 4c,d with a maximum of ~2.9 μm. From the interpretation in 3D, length 3D and width 3D of segmented voids were extracted and computed (SI-1 Fig. S24) with a maximum of ~147 μm for length 3D highlighting the large progression of the lesion in one segmented object. The lowest value of volume arose from single voxels, and this also influenced other measurements. It can be seen Feret shape is high for several segmented objects with a high number of voxels and this confirms the observation previously made with the presence of channels from the demineralisation along the depth (SI-1 Fig. S25). Adding to the full range of data, a highlight is made for higher value of Feret shape and this revealed the locations of longer elongated voids. The influence of the number voxels on the measurement of the Feret shape was previously discussed on the analysis of voids

from a damaged copper cylinder [101]. Additional region in AEC1 and AEC2 are analysed and detailed in SI-1 Fig. S26 and Movie 4.

A complex non-homogeneous demineralisation was noticed and the quantification of the distance of non-demineralised region was computed from the distance field of the spacing between voids (computation of the distance from the nearest neighbour boundary using Euclidian distance metric from the module in Avizo Distance map (outside region is set to 0)), as displayed Figs. 4e,f and 3 c. This highlighted the surface of the tooth, the bottom of the ROI (region 4 previously described) analysed and localised regions where less mineral loss occurred.

Two individual segmented regions were selected, Fig. 5a, and the curvature of the 3D rendering from the first region was seen (Fig. 5b)
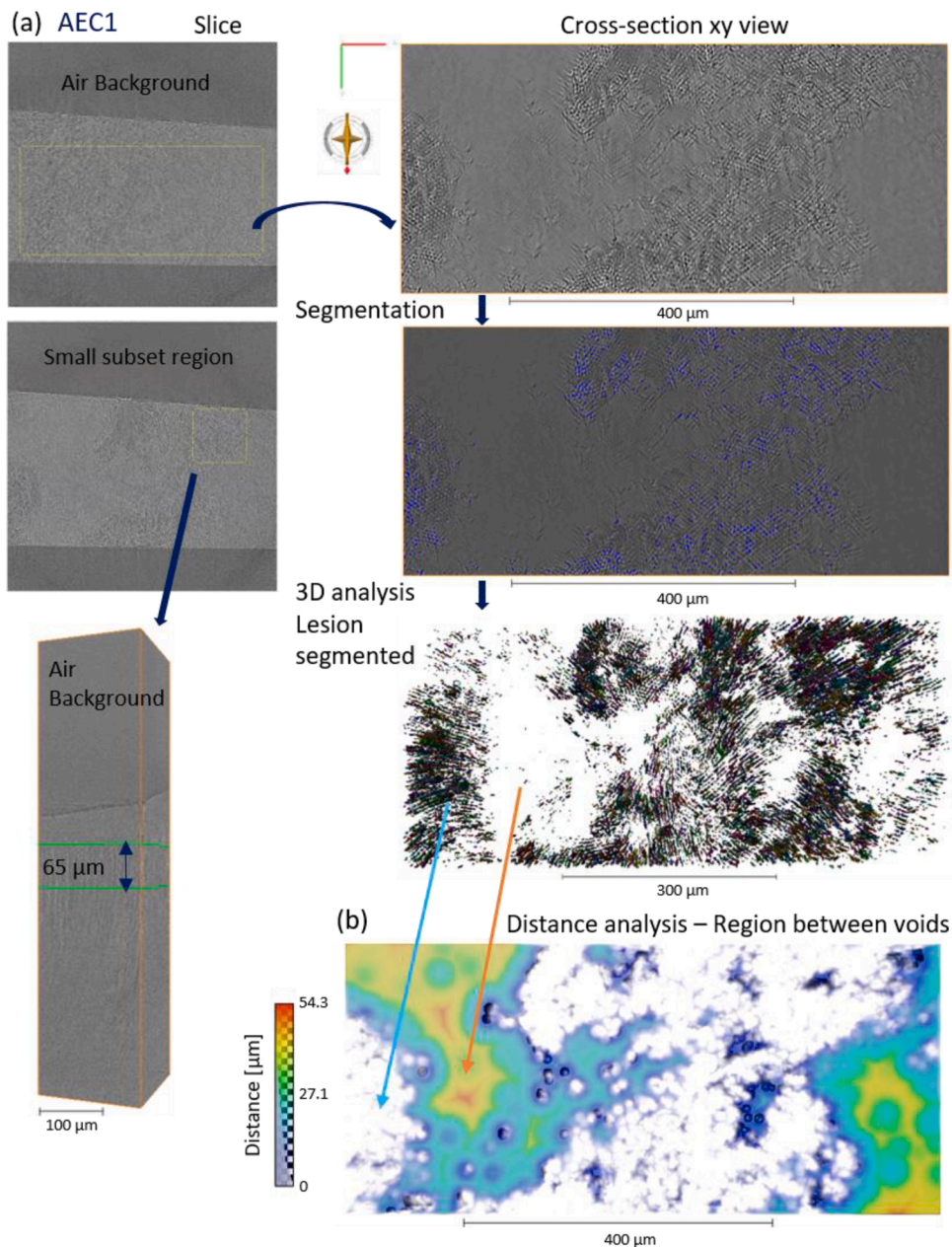
Fig. 3. 3D analysis of a wide region of AEC1. (a) A large subset region (2277 × 1035 × 201 pixels – 739.7 × 336.05 × 65 μm³) after filtering, thresholding (blue colour) and 3D label analysis of the mineral loss region, and the location of the region along the depth of the sample, (b) Volume rendering of the computation of the Euclidian distance of the region between voids, colour map assigned to the distance in μm. (For interpretation of the references to colour in the Figure, the reader is referred to the web version of this article).

along with the connections and the thickness of the voids, Fig. 5b,c. The length 3D of the first region was found to be 121.72 μm. It showed a clear appearance along the depth where a connected region was located and it highlighted the difficulty for potential repair. From the second region, the alignment of the mineral loss region was observed with three major demineralised channels (Fig. 5c). This highlighted the potential of this method for tracking rod structure.

3.5. Analysis of the EC1 sample in 2D and 3D

Here the same methods as applied previously for the advanced enamel caries samples were used, and etching patterns type 1 and type 2 could be resolved in EC1. This study did not aim to generate a general comparison between lesions, but to highlight the features which could be resolved and analysed in a different lesion.

Fig. 6 displays slices from EC1 and 3D analysis of subregions. From the view of the slices, it was found that demineralisation affected the rod (type 1) and the inter-rod phases (type 2), with details differing from the

two advanced enamel caries samples. Etching pattern type 3 could be identified corresponding with a mixture of both previous types (Fig. 6c). While etching pattern type 4 was related to the presence of pits in the enamel and appeared to be present (Fig. 6a). Regions were also found (Fig. 6a), which could be assigned to type 5 following the denomination of Galil and Wright and also later mentioned by Hobson et al., assigned to smooth surfaces, in addition to the three etching patterns reported by Silverstone et al. [54,55,102]. Here, a clear identification of etching patterns type 2 and 1 was resolved. From a region with mainly type 2 demineralisation (see details Fig. 6b,c), following the grey value analysis over a line profile over few rods, the profile of the lesion relating to absorption could be estimated and microstructure of the enamel could be determined. It was found that inter-rod was with the lowest grey values, then surrounding by a non-demineralised region and in the middle a low decrease of grey values suggested to be the demineralisation of the rod core (a low degree of type 2 demineralisation). 3D rendering of the inter-rod being demineralised with the thickness of the non-demineralised region, confirmed the dimension of the enamel rod,
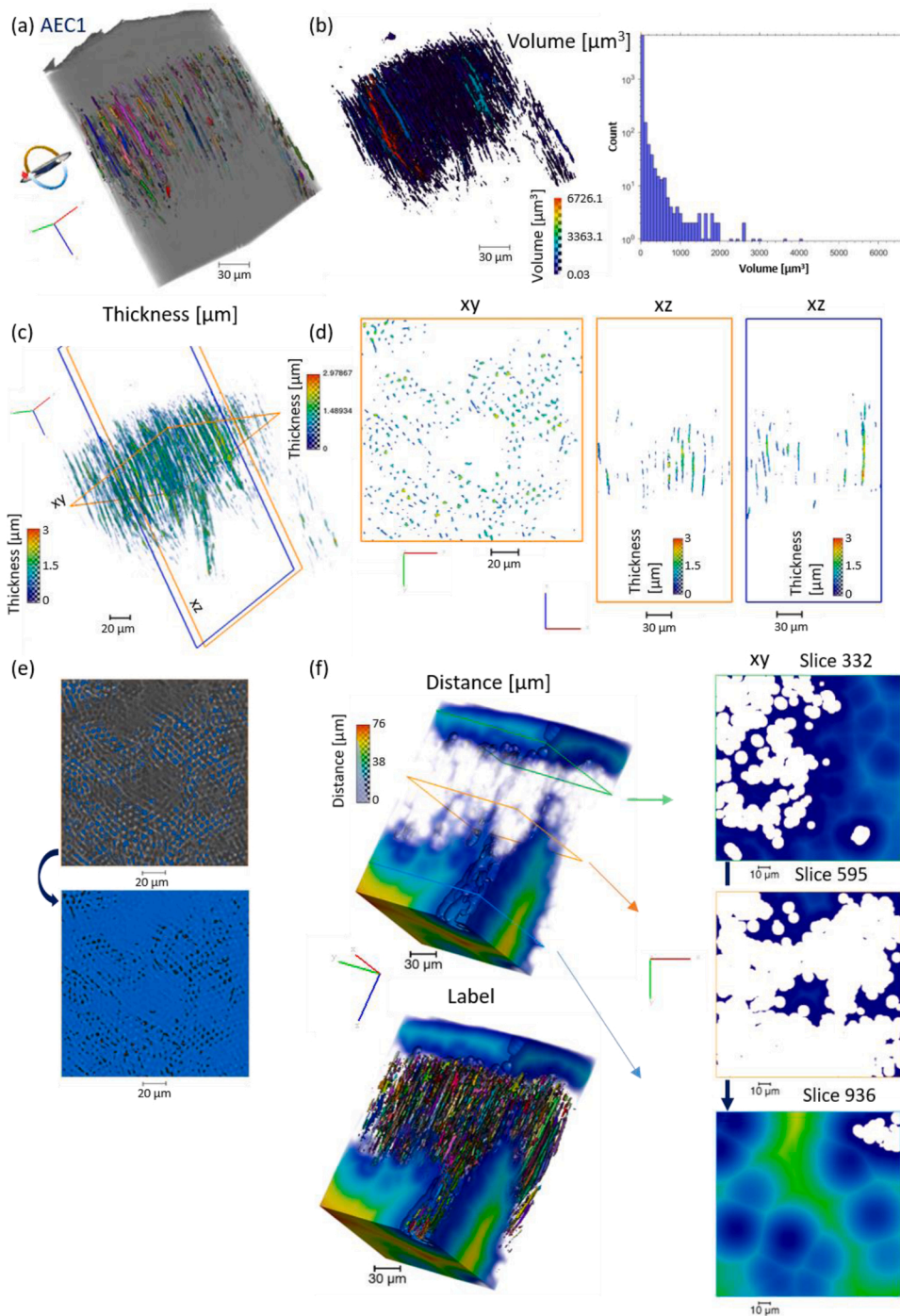
Fig. 4. Analysis of a subregion of AEC1, volume and thickness of the demineralised region, and distance of the non-demineralised region. (a) Volume rendering of the tooth region of AEC1 with an overlap of the demineralisation region segmented, with different colours assigned to individual separated regions and the 3D rendering of the volume of each regions in (b) with histogram of the results. (c) Thickness of the previous 3D demineralised region with the highlight of one slice xy and two slices xz displayed in (d). (e) Slices showing the segmented region for the mineral loss and the spacing between voids extracted using Arithmetic module. (f) Volume rendering of the distance with and without the labels and three extracted slices along the depth of the enamel, locations highlighted in the 3D rendering.

head and tail, and also the possibility to see what is sometimes described as 'fish scale', which was then correlated with a region in an etched slice seen using SEM, with mainly type 2 demineralisation (Fig. 6d,e). Inhomogeneity of demineralisation was noticed from the different dissolution of rods and inter-rods in a similar manner to that seen in advanced enamel lesions. But here, the shape of the rod with inter-rod could be seen, with some rods highly distorted (Fig. 6d). From the type 1 demineralisation (Fig. 6f), long channels were identified, with connections, which were also identified in the two advanced enamel carious samples. The location of demineralisation could be at the inter-rod phase then going to the rod and the centre of the rod to the rod.

Fig. 7a,b shows that two demineralised regions referred to as 'rod 1' and 'rod 2' globally oriented in the same way following barycenter analysis, have differences in the demineralisation dimension but also present some similarities. Both seem to have a less demineralised region between two advanced voids. Fig. 7c shows the length and area of the demineralisation region of rods as a function of depth from a small region in EC1 following the computation in 2D of each slice analysed. In a single rod, the demineralisation is not homogenous along the depth and a decrease of the lesion extent was found and the most severe decrease in dissolution noticed at a depth ~23.4 μm in the two demineralised regions. For the rod 1 (displayed in blue), the second part was segmented considering a straight rod. It is worth noting that with an increase in the depth of the sample, a decrease of the diameter of the rods was first found followed by an increase in the diameter, highlighting the difficulty to perform remineralisation. It was not possible to confirm if this
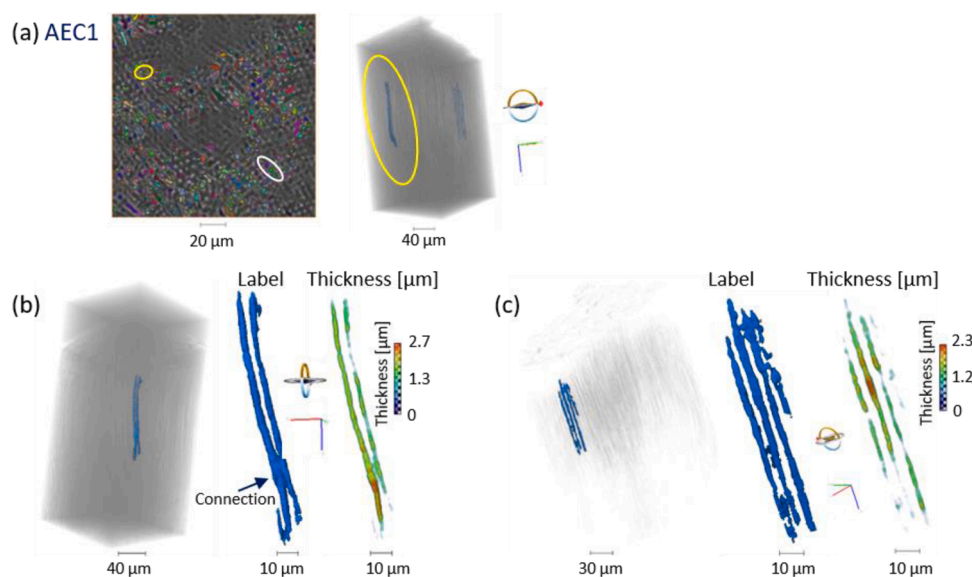
Fig. 5. 3D rendering of isolated demineralised region in AEC1. (a) The display of one slice and two regions extracted with their location in 2D and 3D. (b) 3D representation of the first region and the thickness computed. (c) Representation of the second region with its thickness.

variation was from the demineralisation followed by remineralisation of the rod or just demineralisation. The presence of a less demineralised plane is also seen in Figs. 7,8. In the present study, with high-resolution it was possible to track the demineralisation from rod to inter-rod, this is illustrated Fig. 8 where we further perform analysis of one rod.

To further illustrate the presence of lesions both within rods and inter-rod phases and the possibility to analyse it with sufficient quality, two regions were identified. Fig. 8 shows a virtual section of a reconstructed dataset and the visualisation of the 3D analysis of the rod and inter-rod from one isolated rod along the thickness of the tooth. The image provides a clear identification of the lesion being at the periphery, then propagation of the lesion in the rod, which is the main location going further in the tooth. A plane with a minimal lesion can be detected, and connections between rods and inter-rod were identified (see full dataset SI-1 Movie 5). For the lesion in the rod, the dimension was not constant, representing the computational thickness, revealing either preferential demineralisation or remineralisation or both, although this could not be determined inequivocally.

The analysis in Fig. 8b depicts the quantification of the area of the lesion and spacing from a subregion to determine the profile of the lesion. Three regions could be distinguished, in the first slices, the main contribution for the lesion is the inter-rod, leaving spacing less affected in the rod, indicated by a higher area. In a second step, the increase in area of the lesion was correlated with the increase in demineralisation in the rod while still some remaining of inter-rod contribution, it was also possible to reveal connections between these two structures and in the third step, the lesion in the inter-rod, was not as severe as the first region. 3D rendering of the region is shown in Fig. 8c, where one rod demineralised is highlighted, and the spacing of the lesion and spacing computed. Gradual variation of the lesion with depth was observed.

Taken together, these results where the structure of the lesion in an isolated rod is found to go beyond the traditionally described regions of early carious enamel described by Goldberg (*surface zone*, *subsurface* layer (also referred as *body of the lesion*), *dark* zone and *translucent* zone) [29,103], and the profile of demineralisation (either artificial or natural) which can be observed [29,104]. Here, additional regions were found in the rod itself, with variation of the degree of lesion, in core, inter-rod, and location with minimal demineralisation preceding high demineralisation.

Taken together, this demonstrated the success of the use of this non-destructive approach to study the microstructure of demineralised

human enamel with high-resolution, additional etched samples were also analysed showing the level of details (SI-1 Fig. S27). In term of comparison for the level of details in 2D and 3D (qualitatively and quantitatively) presented here from synchrotron X-ray tomography, there have been no other reports on actual human dental caries samples to our knowledge. Dowker et al. using a synchrotron, with a voxel size of 1.9 µm [41] could image striae and rods, but the analysis of demineralisation in the inter-rods substance was at the limit of the spatial resolution. This requires high-resolution and additional details can found in SI-2 Fig. S2 and Table S1. In Ackermann et al., supposedly inter-rods and rods (seen as channels) were detected depending on the locations in the samples, however the resolution was not mentioned and no quantitative analysis was reported [105]. High-resolution of the structure of the enamel (below 1 µm), was previously identified using synchrotron tomography in absorption on artificial demineralised sample (this study and our previous work [10]) and with phase contrast, and in terms of examples: modern human [106] (minor carious lesions in the roots could be present but this was not the main features analysed), in hominoid, *Australopithecus, Paranthropus* [107–110], *Homo* [111,112], Neanderthal [113,114] (Tafforeau et al. were the first to segment individual rods from the surface to almost the dentine-enamel junction), *Sinanthropus officinalis* [115] from Pleistocene hominins, and animal, for instance, *Rudapithecus hungaricus* [116], orangutan [108], chimpanzee [113], fossil of a *Rhinoceros sondaicus* down to voxel size of 0.28 µm using holotomography [45].

4. Conclusion

This study demonstrated the feasibility to study carious demineralisation of enamel, and its associated etching patterns, by 3D tomography at high-resolution with a large field of view to quantify fine details in the lesions. Although this analysis required large datasets (~24.7 GB of data in 16 bits), 2D and 3D reconstruction and analysis were carried out and demonstrated the potential use of this powerful tool.

In the analysed samples, a difference in the distribution of etching patterns was noticed in the carious samples. In EC1, rod and inter-rod demineralisation could be resolved and it was possible (for the first time) to extract profiles of the demineralisation using 3D X-ray tomography. More samples and analysis will be required to confirm these observations and distinctions in the progress of the lesion. For instance, statistical analysis of the dimension of individual rods from 2D section
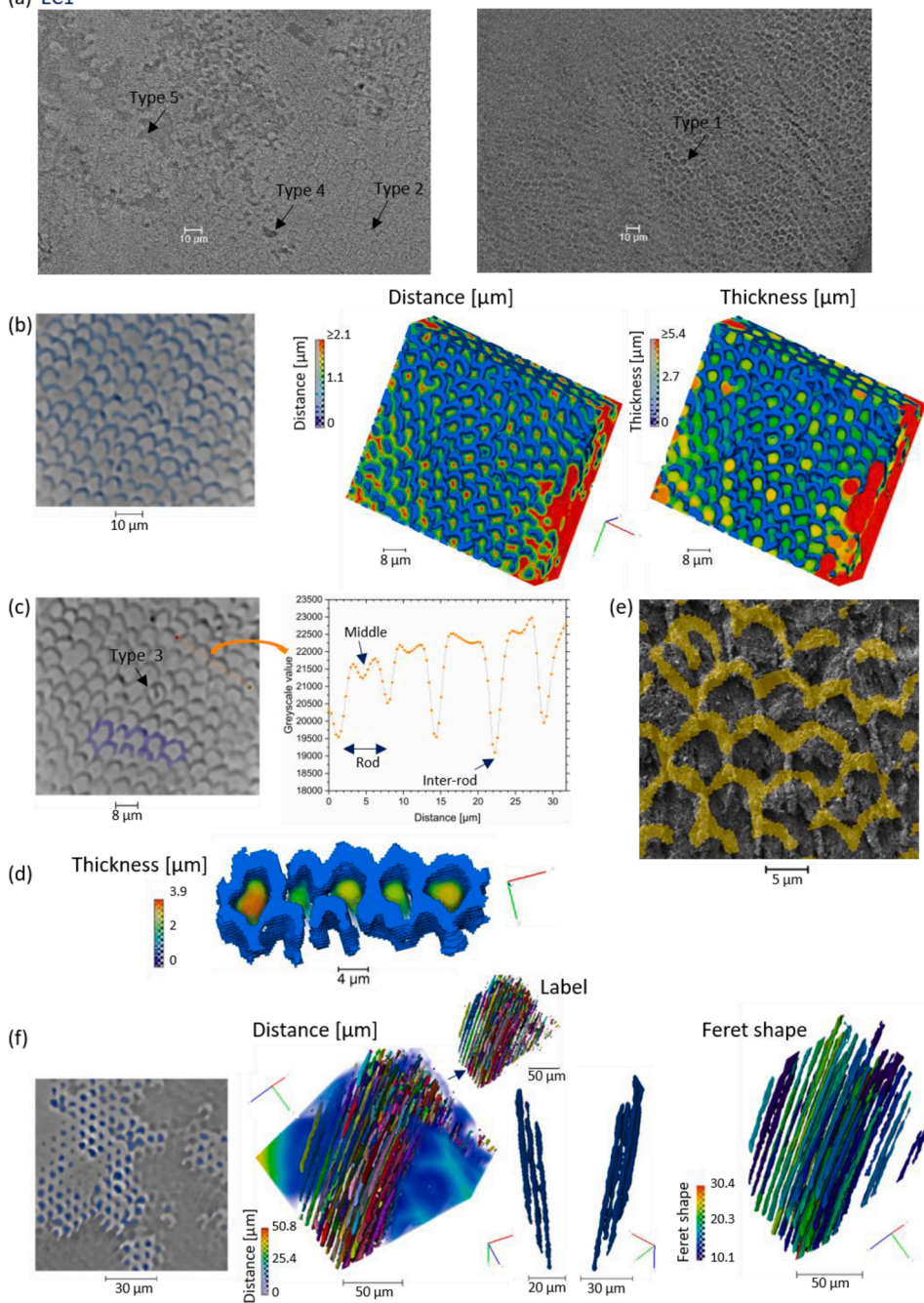
Fig. 6. Evaluation of the lesion in EC1 with a extend highlight on etching pattern type 2 and 1. (a) Raw data from two slices of EC1 showing the demineralisation area: wide region, inter-rods and core of the rods, with an illustration of etching patterns type 1 – type 2 – type 4 – type 5 and type 3 being displayed in (c). (b) Subregion of a volume of 80.925 × 71.175 × 32.5 µm³ (250 × 220 × 101 pixels), type 2 mainly found, with the analysis of the inter-rod highlighted in blue and then 3D rendering of the segmented region, distance field and thickness of the spacing, automatic thresholding carried out. (c) Analysis of few inter-rod from type 2 and rods, line profile and extraction from their inter-rods (using segmentation editor) of five rods, which were represented in 3D with the thickness of the non-demineralised segmented region, being the rods (d). (e) Overlap of the binarised region of (b) with a SEM image of etched slice sample. The overlap was not completely matched arising from the disparity in rod shapes. (f) From left to right, analysis of the demineralisation of the rods, shown with an xy view on a reconstructed slice, mainly type 1 with additional connections demineralised, 3D rendering of the distance of the spacing with an overlap of the segmented region (individual rendering displayed on the top). Illustration of one region view under two orientations and Feret shape factor of the lesion. The values of shape factor were filtered to show only high value, highlighting the trajectory of these volumes. (For interpretation of the references to colour in the Figure, the reader is referred to the web version of this article).

following the orientation of the rods could be performed and this could also add comparison in different lesions. However, the level of spatial resolution possible and statistical evaluation brings new details on the carious research.

The data acquired from the reconstruction of 3D tomography may be useful as input to validate numerical modelling of enamel dissolution. In the current work, we examined static samples at an end time point; however, the techniques reported here could be translated into *in situ* time-lapse experiments of demineralisation with flow and potentially remineralisation to decipher the process in detail and analyse the history of the process. These future studies could use the fast acquisition (less than 30 min per acquisition) to observe the evolution of the structure of enamel at the sub-micron scale. The 3D observation of the lesion and the thickness analysis of the region close to the surface of the carious sample less demineralised than the inner region could be further characterised

to understand the elemental composition (*e.g.* elemental analysis and spectroscopy), the orientation of the HAp and the mechanical properties in different degree of severity of caries lesions.

Finally, our method presents a new characterisation technique for caries research that could be applied to other research in different locations of teeth, such as dentine, with or without caries and other dental diseases.
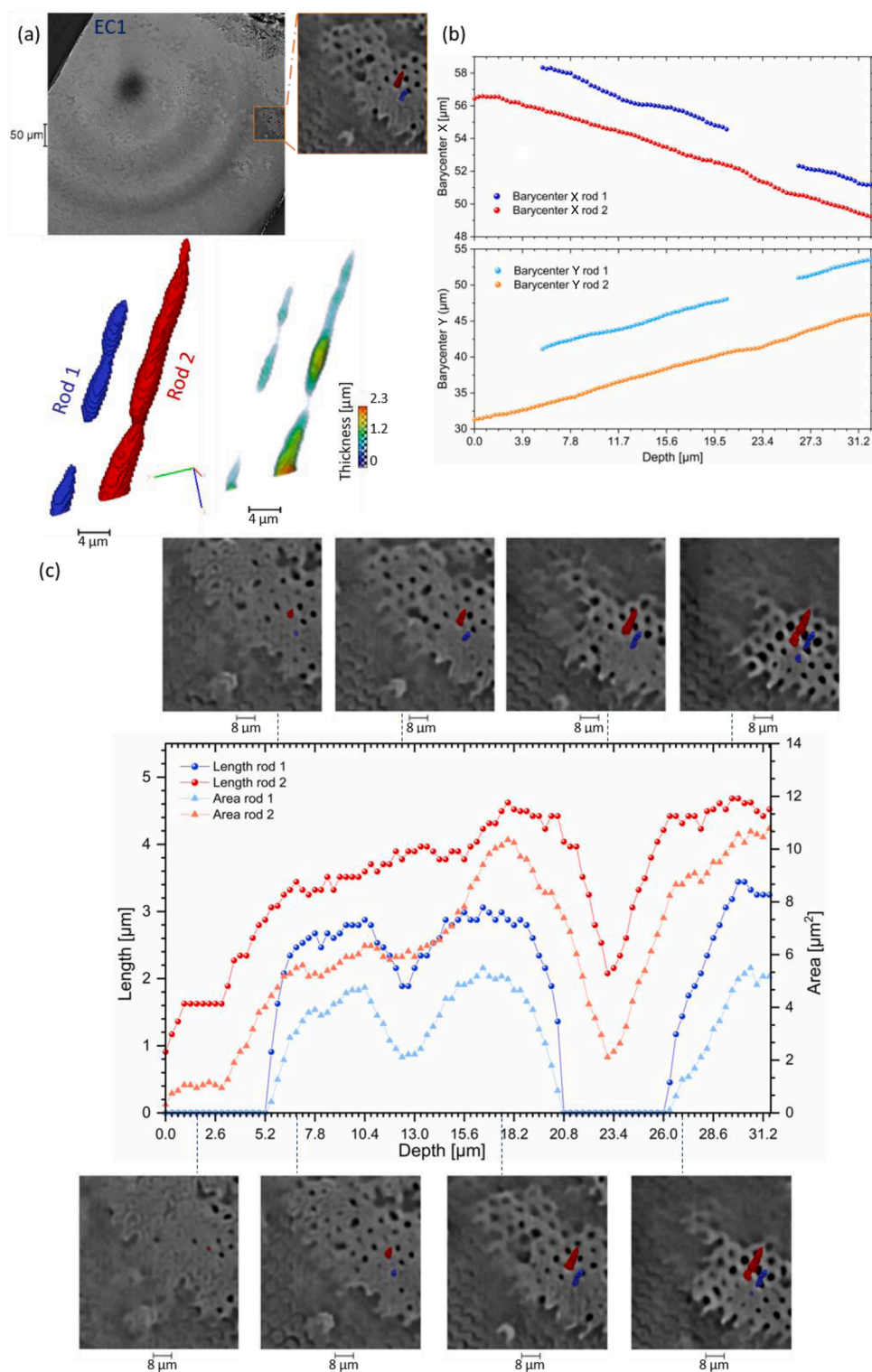
CRediT authorship contribution statement

Fig. 7. Visualisation and quantitative analysis of two separated segmented region in EC1 and their location. (a) 2D slice of the EC1 sample filtered with median and non-local means (1650×1550 pixels – 535.93×503.43 μm^2) and a subregion analysed (with the 3D rendering of the demineralisation regions with the corresponding thickness for two subregions referred to as 'rod 1' and 'rod 2'. (b) Barycenter in x and y of the two segmented regions from the computation of each slice as a function of the depth (0 being the beginning for this region) highlighting nearly similar orientation, (c) Area and length extracted for each slice. This shows the sharp details from two rods where the demineralisation can be tracked. For rod 1, the second part was segmented in continuity of the first region. For both regions, the segmentation was done using segmentation editor and brush to isolate the region of interest slice by slice. The full region is $215 \times 234 \times 131$ pixels ($69.6 \times 75.7 \times 42.6$ μm^3). A complete view of each slice and demineralisation region was extracted (see details SI-1 Movie 5).

Data availability statement

Data collected and interpreted in this study is maintained by the authors and can be made available upon request.
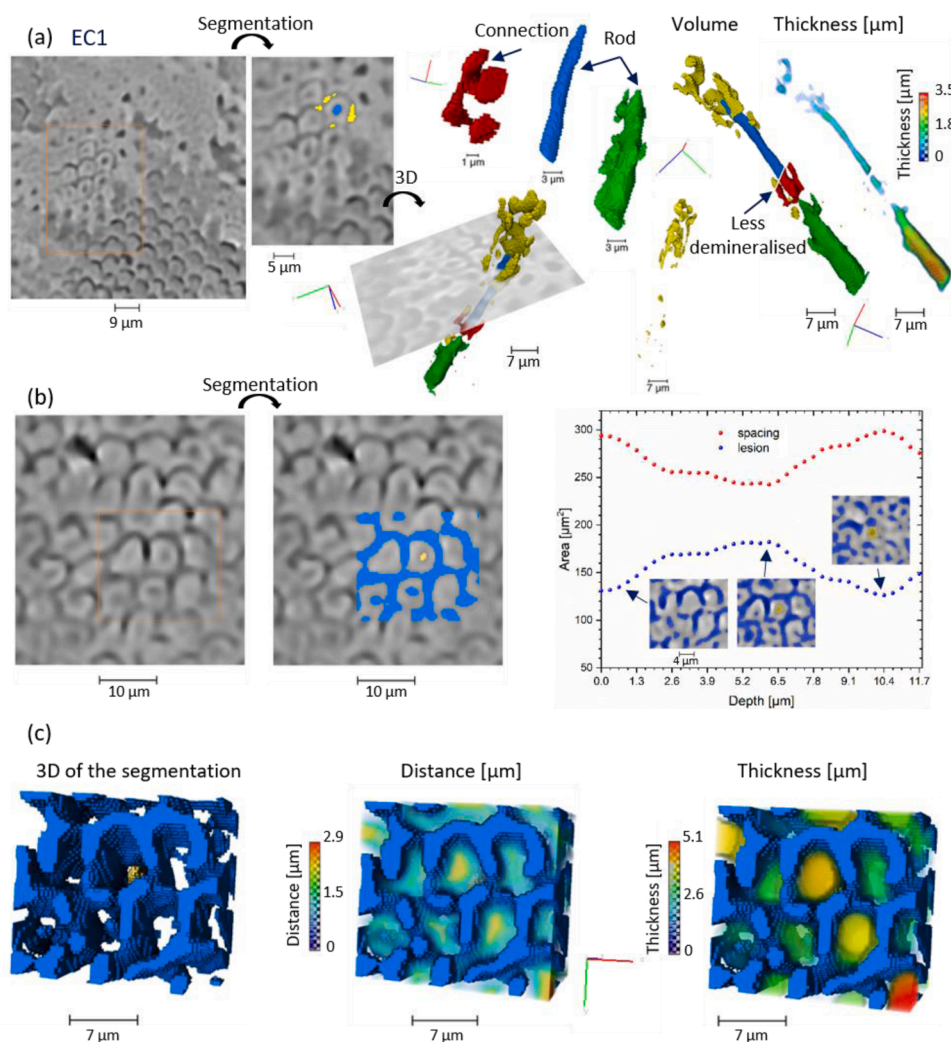
Fig. 8. 3D reconstructed images and 2D analysis of rod and inter-rod, allows visual assessment of the demineralisation location in EC1. (a) Reconstructed slice of EC1 showing lesion in inter-rod and rod, subregion (111 × 148 × 221 pixels) where one rod (in blue) and inter-rod (in yellow) was extracted and segmented (manual segmentation with same range of grey values slice by slice), and 3D representation of the volume with colour assigned for different regions, in red a connection between rod and inter-rod was observed, and then in green the bottom of the volume with the rod's dimension larger than the blue region, the slice was kept to indicate the position (additional details SI-1 Movie 6). (b) Illustration of another region, and a subregion (67 × 60 × 37 pixels) was extracted and the area of the lesion and spacing was computed for each slice as a function of depth (depth of 0 μm was for the first slice of this region), the range of grey values used was the same for all the slices for a direct comparison. (c) 3D rendering of the lesion with an overlap of the distance and thickness of the spacing (the progression of the lesion with depth is shown in SI-1 Movie 7). (For interpretation of the references to colour in the Figure, the reader is referred to the web version of this article).

Declaration of Competing Interest

The authors declare that they have no competing interests.

Acknowledgements

Appendix A. Supplementary data

Supplementary material related to this article can be found in the online version at https://doi.org/10.1016/j.mtcomm.2021.102418.

References

[1] O. Fejerskov, E.A.M. Kidd, B. Nyvad, V. Baelum, Defining the disease: an introduction, in: O. Fejerskov, Edwina A.M. Kidd (Eds.), Dental Caries the Disease and Its Clinical Management, 2008, pp. 3–6. Ch. 1.

[2] S.L. James, et al., Global, regional, and national incidence, prevalence, and years lived with disability for 354 diseases and injuries for 195 countries and territories, 1990–2017: a systematic analysis for the Global Burden of Disease Study 2017, Lancet 392 (2018) 1789–1858, https://doi.org/10.1016/S0140-6736(18)32279-7.

[3] S. Listl, J. Galloway, P.A. Mossey, W. Marcenes, Global economic impact of dental diseases, J. Dent. Res. 94 (2015) 1355–1361, https://doi.org/10.1177/0022034515602879.

[4] S.D. Forssten, M. Björklund, A.C. Ouwehand, *Streptococcus mutans*, caries and simulation models, Nutrients 2 (2010) 290–298, https://doi.org/10.3390/nu2030290.

[5] D. Kim, et al., Spatial mapping of polymicrobial communities reveals a precise biogeography associated with human dental caries, Proc. Natl. Acad. Sci. (2020), 201919099, https://doi.org/10.1073/pnas.1919099117.

[6] G. Hwang, et al., Simultaneous spatiotemporal mapping of *in situ* pH and bacterial activity within an intact 3D microcolony structure, Sci. Rep. 6 (2016) 32841, https://doi.org/10.1038/srep32841.

[7] W.J. Loesche, Role of *Streptococcus mutans* in human dental decay, Microbiol. Rev. 50 (1986) 353–380.

[8] P.D. Marsh, A. Moter, D.A. Devine, Dental plaque biofilms: communities, conflict and control, Periodontology 55 (2000) 16–35, https://doi.org/10.1111/j.1600-0757.2009.00339.x (2011).

[9] K.A. DeRocher, et al., Chemical gradients in human enamel crystallites, Nature 583 (2020) 66–71, https://doi.org/10.1038/s41586-020-2433-3.

[10] E. Salvati, et al., Finite element modelling and experimental validation of enamel demineralisation at the rod level, J. Adv. Res. 29 (2021) 167–177, https://doi.org/10.1016/j.jare.2020.08.018.

[11] J.A. Saavedra-Abril, et al., Dental multisection CT for the placement of oral implants: technique and applications, Radiographics 30 (2010) 1975–1991, https://doi.org/10.1148/rg.307105026.

[12] A. Basu, K. Rothermund, M.N. Ahmed, F.N. Syed-Picard, Self-assembly of an organized cementum-periodontal ligament-like complex using scaffold-free tissue engineering, Front. Physiol. 10 (2019) 1–9, https://doi.org/10.3389/fphys.2019.00422.

[13] J.D.B. Featherstone, A. Lussi, Understanding the chemistry of dental erosion, Monogr. Oral Sci. 20 (2006) 66–76, https://doi.org/10.1159/000093351.

[14] E. Bonte, N. Deschamps, M. Goldberg, V. Vernois, Quantification of free water in human dental enamel, J. Dent. Res. 67 (1988) 880–882, https://doi.org/10.1177/00220345880670051701.

[15] T. Baumann, T.S. Carvalho, A. Lussi, The effect of enamel proteins on erosion, Sci. Rep. 5 (2015) 15194, https://doi.org/10.1038/srep15194.

[16] Y. Bai, et al., Protein nanoribbons template enamel mineralization, Proc. Natl. Acad. Sci. 117 (2020) 19201–19208, https://doi.org/10.1073/pnas.2007838117.

[17] G. Daculsi, J. Menanteau, L.M. Kerebel, D. Mitre, Length and shape of enamel crystals, Calcif. Tissue Int. 36 (1984) 550–555, https://doi.org/10.1007/BF02405364.

[18] S. Risnes, C. Li, On the method of revealing enamel structure by acid etching. Aspects of optimization and interpretation, Microsc. Res. Tech. 82 (2019) 1668–1680, https://doi.org/10.1002/jemt.23333.

[19] S. Risnes, M. Saeed, A. Sehic, Scanning electron microscopy (SEM) methods for dental enamel, in: Petros Papagerakis (Ed.), Odontogenesis: Methods and Protocols, Springer, New York, 2019, pp. 293–308. Ch. 27.

[20] F.-Z. Cui, J. Ge, New observations of the hierarchical structure of human enamel, from nanoscale to microscale, J. Tissue Eng. Regen. Med. 1 (2007) 185–191, https://doi.org/10.1002/term.21.

[21] V. Uskoković, M.K. Kim, W. Li, S. Habelitz, Enzymatic processing of amelogenin during continuous crystallization of apatite, J. Mater. Res. 23 (2008) 3184–3195, https://doi.org/10.1557/JMR.2008.0387.

[22] L. Wang, et al., A new model for nanoscale enamel dissolution, J. Phys. Chem. B 109 (2005) 999–1005, https://doi.org/10.1021/jp046451d.

[23] J. Ge, F.Z. Cui, X.M. Wang, H.L. Feng, Property variations in the prism and the organic sheath within enamel by nanoindentation, Biomaterials 26 (2005) 3333–3339, https://doi.org/10.1016/j.biomaterials.2004.07.059.

[24] L.H. He, M.V. Swain, Understanding the mechanical behaviour of human enamel from its structural and compositional characteristics, J. Mech. Behav. Biomed. Mater. 1 (2008) 18–29, https://doi.org/10.1016/j.jmbbm.2007.05.001.

[25] J.D. Haines, Physical properties of human tooth and enamel sheath material under load, J. Biomech. 1 (1968) 117–125.

[26] O. Duverger, E. Beniash, M.I. Morasso, Keratins as components of the enamel organic matrix, Matrix Biol. 52-54 (2016) 260–265, https://doi.org/10.1016/j.matbio.2015.12.007.

[27] S. Risnes, S.Ö. Stölen, Uncoated specimen of human enamel observed in the scanning electron microscope, Eur. J. Oral Sci. 89 (1981) 205–212, https://doi.org/10.1111/j.1600-0722.1981.tb01672.x.

[28] A.H. Meckel, W.J. Griebstein, R.J. Neal, Structure of mature human dental enamel as observed by electron microscopy, Arch. Oral Biol. 10 (1965) 775–783.

[29] M. Goldberg, in: Michel Goldberg (Ed.), Enamel Softening (Dental Erosion) - Enamel Etching - the Early Enamel Carious Lesion in *Understanding Dental Caries*, 2016. Ch. 2.4.

[30] A.M. Kelly, et al., Measuring the microscopic structures of human dental enamel can predict caries experience, J. Pers. Med. 10 (2020) 5, https://doi.org/10.3390/jpm10010005.

[31] S. Risnes, C. Li, Aspects of the final phase of enamel formation as evidenced by observations of superficial enamel of human third molars using scanning electron microscopy, Arch. Oral Biol. 86 (2018) 72–79, https://doi.org/10.1016/j.archoralbio.2017.11.008.

[32] M. Hørsted, O. Fejerskov, M.J. Larsen, A. Thylstrup, The structure of surface enamel with special reference to occlusal surfaces of primary and permanent teeth, Caries Res. 10 (1976) 287–296, https://doi.org/10.1159/000260209.

[33] A.J. Gwinnett, The ultrastructure of the "prismless" enamel of permanent human teeth, Arch. Oral Biol. 12 (1967) 381–393, https://doi.org/10.1016/0003-9969(67)90022-1.

[34] A. Nanci, Enamel: composition, formation, and structure, in: Antonio Nanci (Ed.), Ten Cate's Oral Histology, 8th edition, 2012. Ch. 7.

[35] S. Risnes, A scanning electron microscope study of the three-dimensional extent of Retzius lines in human dental enamel, Eur. J. Oral Sci. 93 (1985) 145–152, https://doi.org/10.1111/j.1600-0722.1985.tb01323.x.

[36] A. Boyde, The development of enamel structure, Proc. R. Soc. Med. 60 (1967) 923–928.

[37] R.S. Lacruz, S. Habelitz, J.T. Wright, M.L. Paine, Dental enamel formation and implications for oral health and disease, Physiol. Rev. 97 (2017) 939–993, https://doi.org/10.1152/physrev.00030.2016.

[38] S. Risnes, Structural characteristics of staircase-type retzius lines in human dental enamel analyzed by scanning electron microscopy, Anat. Rec. 226 (1990) 135–146, https://doi.org/10.1002/ar.1092260203.

[39] R.K. Bharath, Enamel, Ch. 2. Fundamentals of Oral Anatomy, Physiology and Histology, 2019, pp. 16–32.

[40] A.D. Beynon, M.C. Dean, D.J. Reid, On thick and thin enamel in hominoids, Am. J. Phys. Anthropol. 86 (1991) 295–309, https://doi.org/10.1002/ajpa.1330860216.

[41] S.E.P. Dowker, J.C. Elliott, G.R. Davis, R.M. Wilson, P. Cloetens, Synchrotron X-ray microtomographic investigation of mineral concentrations at micrometre scale in sound and carious enamel, Caries Res. 38 (2004) 514–522, https://doi.org/10.1159/000080580.

[42] C.D. Lynch, V.R. O'Sullivan, P. Dockery, C.T. McGillycuddy, A.J. Sloan, Hunter-Schreger Band patterns in human tooth enamel, J. Anat. 217 (2010) 106–115, https://doi.org/10.1111/j.1469-7580.2010.01255.x.

[43] J. Wilmers, S. Bargmann, Nature's design solutions in dental enamel: uniting high strength and extreme damage resistance, Acta Biomater. 107 (2020) 1–24, https://doi.org/10.1016/j.actbio.2020.02.019.

[44] R.A. Harper, et al., Acid-induced demineralisation of human enamel as a function of time and pH observed using X-ray and polarised light imaging, Acta Biomater. 120 (2021) 240–248, https://doi.org/10.1016/j.actbio.2020.04.045.

[45] P. Tafforeau, I. Bentaleb, J.-J. Jaeger, C. Martin, Nature of laminations and mineralization in rhinoceros enamel using histology and X-ray synchrotron microtomography: potential implications for palaeoenvironmental isotopic studies, Palaeogeogr. Palaeoclimatol. Palaeoecol. 246 (2007) 206–227, https://doi.org/10.1016/j.palaeo.2006.10.001.

[46] R.Z. LeGeros, Chemical and crystallographic events in the caries process, J. Dent. Res. 69 (1990), https://doi.org/10.1177/00220345900690S113.

[47] N.B. Pitts, et al., Dental caries, Nat. Rev. Dis. Primers 3 (2017) 17030, https://doi.org/10.1038/nrdp.2017.30.

[48] W.H. Bowen, Dental caries - not just holes in teeth! A perspective, Mol. Oral Microbiol. 31 (2016) 228–233, https://doi.org/10.1111/omi.12132.

[49] J.D.B. Featherstone, The science and practice of caries prevention, J. Am. Dent. Assoc. 131 (2000) 887–899, https://doi.org/10.14219/jada.archive.2000.0307.

[50] M.E. Dickinson, K.V. Wolf, A.B. Mann, Nanomechanical and chemical characterization of incipient *in vitro* carious lesions in human dental enamel, Arch. Oral Biol. 52 (2007) 753–760, https://doi.org/10.1016/j.archoralbio.2007.02.007.

[51] T.T.Y. Huang, L.H. He, M.A. Darendeliler, M.V. Swain, Nano-indentation characterisation of natural carious white spot lesions, Caries Res. 44 (2010) 101–107, https://doi.org/10.1159/000286214.

[52] C. Robinson, S. Connell, J. Kirkham, R. Shore, A. Smith, Dental enamel—a biological ceramic: regular substructures in enamel hydroxyapatite crystals revealed by atomic force microscopy, J. Mater. Chem. 14 (2004) 2242–2248, https://doi.org/10.1039/B401154F.

[53] L.N. Hashizume, K. Shinada, Y. Kawaguchi, Y. Yamashita, Sequence of ultrastructural changes of enamel crystals and *Streptococcus mutans* biofilm in early enamel caries *in vitro*, J. Med. Dent. Sci. 49 (2002) 67–75.

[54] L.M. Silverstone, C.A. Saxton, I.L. Dogon, O. Fejerskov, Variation in the pattern of acid etching of human dental enamel examined by scanning electron microscopy, Caries Res. 9 (1975) 373–387, https://doi.org/10.1159/000260179.

[55] K.A. Galil, G.Z. Wright, Acid etching patterns on buccal surfaces of permanent teeth, Pediatr. Dent. 1 (1979) 230–234.

[56] B.B. Cerci, L.S. Roman, O. Guariza-Filho, E.S. Camargo, O.M. Tanaka, Dental enamel roughness with different acid etching times: atomic force microscopy study, European J. Gen. Dent. 1 (2012) 187–191, https://doi.org/10.4103/2278-9626.105385.

[57] K.V. Mortimer, T.C. Tranter, A scanning electron microscopy study of carious enamel, Caries Res. 5 (1971) 240–263.

[58] J.W. Simmelink, V.K. Nygaard, Ultrastructure of striations in carious human enamel, Caries Res. 16 (1982) 179–188, https://doi.org/10.1159/000260595.

[59] D.B. Scott, J.W. Simmelink, V. Nygaard, Structural aspects of dental caries, J. Dent. Res. 53 (1974) 165–178, https://doi.org/10.1177/00220345740530020401.

[60] G.A. Kerckaert, Electron microscopy of human carious dental enamel, Arch. Oral Biol. 18 (1973) 751–N757, https://doi.org/10.1016/0003-9969(73)90011-3.

[61] T. Yanagisawa, Y. Miake, High-resolution electron microscopy of enamel-crystal demineralization and remineralization in carious lesions, J. Electron Microsc. (Tokyo) 52 (2003) 605–613.

[62] H.H. Harris, S. Vogt, H. Eastgate, P.A. Lay, A link between copper and dental caries in human teeth identified by X-ray fluorescence elemental mapping, JBIC J. Biol. Inorg. Chem. 13 (2008) 303–306, https://doi.org/10.1007/s00775-007-0321-z.

[63] T. Sui, et al., *In situ* monitoring and analysis of enamel demineralisation using synchrotron X-ray scattering, Acta Biomater. 77 (2018) 333–341, https://doi.org/10.1016/j.actbio.2018.07.027.

[64] H. Deyhle, S.N. White, O. Bunk, F. Beckmann, B. Müller, Nanostructure of carious tooth enamel lesion, Acta Biomater. 10 (2014) 355–364, https://doi.org/10.1016/j.actbio.2013.08.024.

[65] J. Lautensack, et al., *In situ* demineralisation of human enamel studied by synchrotron-based X-ray microtomography – a descriptive pilot-study, Micron 44 (2013) 404–409, https://doi.org/10.1016/j.micron.2012.09.006.

[66] S. Siddiqui, P. Anderson, M. Al-Jawad, Recovery of crystallographic texture in remineralized dental enamel, PLoS One 9 (2014), e108879, https://doi.org/10.1371/journal.pone.0108879.

[67] S. Gaiser, H. Deyhle, O. Bunk, S.N. White, B. Müller, Understanding nano-anatomy of healthy and carious human teeth: a prerequisite for nanodentistry, Biointerphases 7 (2012) 4, https://doi.org/10.1007/s13758-011-0004-8.

[68] H. Deyhle, O. Bunk, B. Müller, Nanostructure of healthy and caries-affected human teeth, Nanomed. Nanotechnol. Biol. Med. 7 (2011) 694–701, https://doi.org/10.1016/j.nano.2011.09.005.

[69] C.K. Egan, et al., Non-invasive imaging of the crystalline structure within a human tooth, Acta Biomater. 9 (2013) 8337–8345, https://doi.org/10.1016/j.actbio.2013.06.018.

[70] R. Ordinola-Zapata, et al., The use of confocal laser scanning microscopy for the study of dentin infection, in: A. Méndez-Vilas, J. Díaz (Eds.), Microscopy: Science,

Technology, Applications and Education, Vol. 3, Formatex Research Center, 2010, pp. 583–589.

[71] P. Ye, H. Yu, M. Houshmandi, Three/four-dimensional (3D/4D) microscopic imaging and processing in clinical dental research, BMC Oral Health 16 (2016) 84, https://doi.org/10.1186/s12903-016-0282-0.

[72] M. Cantoni, L. Holzer, Advances in 3D focused ion beam tomography, MRS Bull. 39 (2014) 354–360, https://doi.org/10.1557/mrs.2014.54.

[73] C.S. Xu, et al., Enhanced FIB-SEM systems for large-volume 3D imaging, Elife 6 (2017), https://doi.org/10.7554/eLife.25916.

[74] N. Cougot, et al., Towards quantitative analysis of enamel erosion by focused ion beam tomography, Dent. Mater. (2018), https://doi.org/10.1016/j.dental.2018.08.304.

[75] F. Yun, et al., Nanoscale pathways for human tooth decay – central planar defect, organic-rich precipitate and high-angle grain boundary, Biomaterials 235 (2020), 119748, https://doi.org/10.1016/j.biomaterials.2019.119748.

[76] J. Reyes-Gasga, J. Hémmerlé, E.F. Brès, Aberration-corrected transmission electron microscopic study of the central dark line defect in human tooth enamel crystals, Microsc. Microanal. 22 (2016) 1047–1055, https://doi.org/10.1017/S1431927616011648.

[77] C. Rau, U. Wagner, Z. Pešić, A. De Fanis, Coherent imaging at the Diamond beamline I13, Physica Status Solidi (a) 208 (2011) 2522–2525, https://doi.org/10.1002/pssa.201184272.

[78] C. Rau, Imaging with coherent synchrotron radiation: X-ray imaging and coherence beamline (I13) at diamond light source, Synchrotron Radiat. News 30 (2017) 19–25, https://doi.org/10.1080/08940886.2017.1364530.

[79] C. Rau, et al., Micro- and nano-tomography at the DIAMOND beamline I13L imaging and coherence, in: B. Müller, G. Wang (Eds.), SPIE Optical Engineering + Applications - Developments in X-Ray Tomography XI, SPIE, San Diego, California, United States, 2017. Volume Proc. of SPIE 10391 103910T-103911-103918.

[80] N.T. Vo, R.C. Atwood, M. Drakopoulos, Radial lens distortion correction with sub-pixel accuracy for X-ray micro-tomography, Opt. Express 23 (2015) 32859–32868, https://doi.org/10.1364/OE.23.032859.

[81] J. Kastner, C. Heinzl, X-ray tomography, in: Nathan Ida, Norbert Meyendorf (Eds.), *Handbook of Advanced Non-Destructive Evaluation*, Springer International Publishing, 2018, pp. 1–72.

[82] R.C. Atwood, A.J. Bodey, S.W.T. Price, M. Basham, M. Drakopoulos, A high-throughput system for high-quality tomographic reconstruction of large datasets at Diamond Light Source, Philos. Trans. Math. Phys. Eng. Sci. 373 (2015), 20140398, https://doi.org/10.1098/rsta.2014.0398.

[83] N. Wadeson, M. Basham, Savu: a Python-based, MPI framework for simultaneous processing of multiple, N-dimensional, large tomography datasets, arXiv preprint arXiv:1610.08015 10 (2016).

[84] D. Gürsoy, F. De Carlo, X. Xiao, C. Jacobsen, TomoPy: a framework for the analysis of synchrotron tomographic data, J. Synchrotron Radiat. 21 (2014) 1188–1193, https://doi.org/10.1107/S1600577514013939.

[85] T. Scientific, User's Guide Avizo Software 2019, 2019.

[86] J. Schindelin, et al., Fiji: an open-source platform for biological-image analysis, Nat. Methods 9 (2012) 676, https://doi.org/10.1038/nmeth.2019.

[87] S.J. Brookes, Using ImageJ (Fiji) to analyze and present X-ray CT images of enamel, in: Petros Papagerakis (Ed.), Odontogenesis: Methods and Protocols, Springer, New York, 2019, pp. 267–291. Ch. 26.

[88] Rasband, W. S. ImageJ, U. S. National Institutes of Health, Bethesda, Maryland, USA, https://imagej.nih.gov/ij/. (1997-2018).

[89] W.H. Walton, Feret's statistical diameter as a measure of particle size, Nature 162 (1948) 329–330, https://doi.org/10.1038/162329b0.

[90] T. Hildebrand, P. Rüegsegger, A new method for the model-independent assessment of thickness in three-dimensional images, J. Microsc. 185 (1997) 67–75, https://doi.org/10.1046/j.1365-2818.1997.1340694.x.

[91] E.I. Pearce, D.G. Nelson, Microstructural features of carious human enamel imaged with back-scattered electrons, J. Dent. Res. 68 (1989) 113–118, https://doi.org/10.1177/00220345890680020301.

[92] L.S. Bell, Identifying postmortem microstructural change to skeletal and dental tissues using backscattered electron imaging, in: Lynne S. Bell (Ed.), Forensic Microscopy for Skeletal Tissues: Methods and Protocols, Humana Press, 2012, pp. 173–190. Ch. 11.

[93] J.M. ten Cate, M.J. Larsen, E.I.F. Pearce, O. Fejerskov, Chemical interactions between the tooth and oral fluids, in: Ole Fejerskov, Edwina A.M. Kidd (Eds.), Dental Caries: The Disease and Its Clinical Management, 2008, pp. 209–231. Ch. 12.

[94] T. Aoba, et al., The intact surface layer in natural enamel caries and acid-dissolved hydroxyapatite pellets, J. Oral Pathol. Med. 10 (1981) 32–39, https://doi.org/10.1111/j.1600-0714.1981.tb01245.x.

[95] J.D.B. Featherstone, Dental caries: a dynamic disease process, Aust. Dent. J. 53 (2008) 286–291, https://doi.org/10.1111/j.1834-7819.2008.00064.x.

[96] O. Ilie, A.G. van Turnhout, M.C.M. van Loosdrecht, C. Picioreanu, Numerical modelling of tooth enamel subsurface lesion formation induced by dental plaque, Caries Res. 48 (2014) 73–89, https://doi.org/10.1159/000354123.

[97] J.A. Arsecularatne, M. Hoffman, An *in vitro* study of the microstructure, composition and nanoindentation mechanical properties of remineralizing human dental enamel, J. Phys. D Appl. Phys. 47 (2014), 315403, https://doi.org/10.1088/0022-3727/47/31/315403.

[98] M. Eisenburger, M. Addy, J.A. Hughes, R.P. Shellis, Effect of time on the remineralisation of enamel by synthetic saliva after citric acid erosion, Caries Res. 35 (2001) 211–215, https://doi.org/10.1159/000047458.

[99] B. Mohanty, D. Dadlani, D. Mahoney, A.B. Mann, Characterizing and identifying incipient carious lesions in dental enamel using micro-Raman spectroscopy, Caries Res. 47 (2013) 27–33, https://doi.org/10.1159/000342432.

[100] T. Ueno, et al., Optical analysis of enamel and dentin caries in relation to mineral density using swept-source optical coherence tomography, J. Med. Imaging Bellingham (Bellingham) 3 (2016), https://doi.org/10.1117/1.JMI.3.3.035507, 035507-035507.

[101] B.M. Patterson, J.P. Escobedo-Diaz, D. Dennis-Koller, E. Cerreta, Dimensional quantification of embedded voids or objects in three dimensions using X-ray tomography, Microsc. Microanal. 18 (2012) 390–398, https://doi.org/10.1017/S1431927611012554.

[102] R.S. Hobson, A.J. Rugg-Gunn, T.A. Booth, Acid-etch patterns on the buccal surface of human permanent teeth, Arch. Oral Biol. 47 (2002) 407–412, https://doi.org/10.1016/S0003-9969(02)00008-0.

[103] M. Goldberg, Deciduous tooth and dental caries, Ann. Pediatr. Child Health 5 (2017) 1120.

[104] G.R. Davis, D. Mills, P. Anderson, Real-time observations of tooth demineralization in 3 dimensions using X-ray microtomography, J. Dent. 69 (2018) 88–92, https://doi.org/10.1016/j.jdent.2017.11.010.

[105] M. Ackermann, et al., Biomimetic transformation of polyphosphate microparticles during restoration of damaged teeth, Dent. Mater. 35 (2019) 244–256, https://doi.org/10.1016/j.dental.2018.11.014.

[106] A. Le Cabec, N.K. Tang, V. Ruano Rubio, S. Hillson, Nondestructive adult age at death estimation: visualizing cementum annulations in a known age historical human assemblage using synchrotron X-ray microtomography, Am. J. Phys. Anthropol. 168 (2019) 25–44, https://doi.org/10.1002/ajpa.23702.

[107] A. Le Cabec, N. Tang, P. Tafforeau, Accessing developmental information of fossil hominin teeth using new synchrotron microtomography-based visualization techniques of dental surfaces and interfaces, PLoS One 10 (2015), e0123019.

[108] P. Tafforeau, T.M. Smith, Nondestructive imaging of hominoid dental microstructure using phase contrast X-ray synchrotron microtomography, J. Hum. Evol. 54 (2008) 272–278, https://doi.org/10.1016/j.jhevol.2007.09.018.

[109] S.K. Suter, C.P.E. Zollikofer, R. Pajarola, Application of tensor approximation to multiscale volume feature representations, in: VMV 2010, 15th International Workshop on Vision, Modeling and Visualization, Siegen, 2010, pp. 1–8.

[110] S.K. Suter, C.P.E. Zollikofer, R. Pajarola, Multiscale Tensor Approximation for Volume Data, Department of Informatics, University of Zürich, 2010.

[111] T.M. Smith, et al., Dental ontogeny in Pliocene and early Pleistocene hominins, PLoS One 10 (2015), e0118118, https://doi.org/10.1371/journal.pone.0118118.

[112] S. Xing, et al., First systematic assessment of dental growth and development in an archaic hominin (genus, *Homo*) from East Asia, Sci. Adv. 5 (2019), eaau0930, https://doi.org/10.1126/sciadv.aau0930.

[113] P. Tafforeau, J.P. Zermeno, T.M. Smith, Tracking cellular-level enamel growth and structure in 4D with synchrotron imaging, J. Hum. Evol. 62 (2012) 424–428, https://doi.org/10.1016/j.jhevol.2012.01.001.

[114] T.M. Smith, et al., Dental evidence for ontogenetic differences between modern humans and Neanderthals, Proc. Natl. Acad. Sci. 107 (2010) 20923–20928, https://doi.org/10.1073/pnas.1010906107.

[115] T.M. Smith, et al., Disentangling isolated dental remains of Asian Pleistocene hominins and pongines, PLoS One 13 (2018), https://doi.org/10.1371/journal.pone.0204737 e0204737-e0204737.

[116] T.M. Smith, P. Tafforeau, J. Pouech, D.R. Begun, Enamel thickness and dental development in Rudapithecus hungaricus, J. Hum. Evol. 136 (2019), 102649, https://doi.org/10.1016/j.jhevol.2019.102649.

[117] C. Besnard, et al., Analysis of *in vitro* demineralised human enamel using multi-scale correlative optical and scanning electron microscopy, and high-resolution synchrotron wide-angle X-ray scattering, Mater. Des. (2021), 109739, https://doi.org/10.1016/j.matdes.2021.109739.